

PUBLISHED VERSION

O. Leav, B. Cazzolato, C. Howard, and B. Mabrouk

Steady-state sound propagation through hot exhaust jets in cooler cross-flow: A computational study

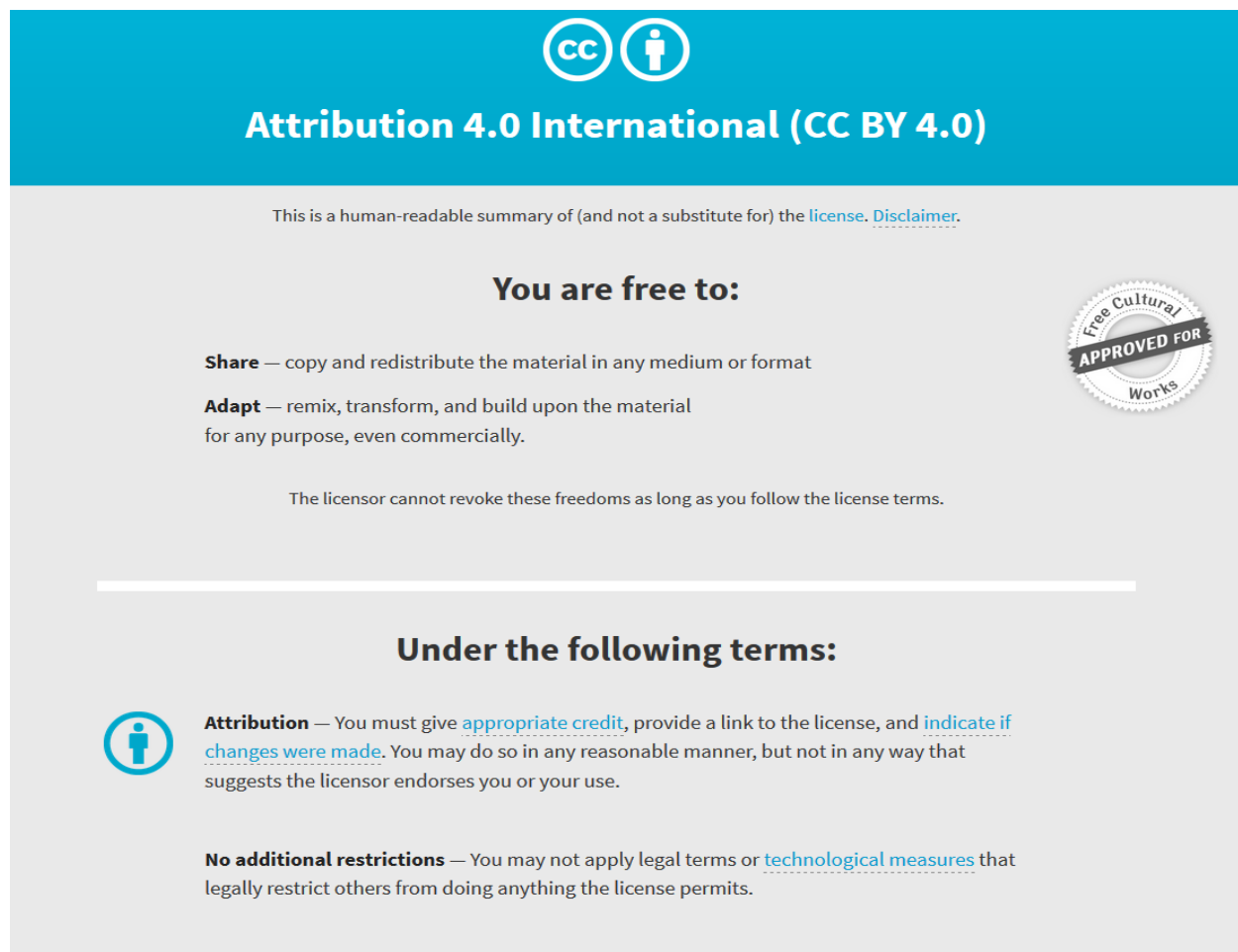
Journal of the Acoustical Society of America, 2023; 154(1):217-231

© 2023 Author(s). All article content, except where otherwise noted, is licensed under a Creative Commons Attribution (CC BY) license (<http://creativecommons.org/licenses/by/4.0/>). Published open access through an agreement with The University of Adelaide School of Electrical and Mechanical Engineering. Journal © 2023 Acoustical Society of America.

Published version: <http://dx.doi.org/10.1121/10.0020069>

PERMISSIONS

<http://creativecommons.org/licenses/by/4.0/>



The image shows the Creative Commons Attribution 4.0 International (CC BY 4.0) license graphic. It features a blue header with the CC logo and a person icon, followed by the text "Attribution 4.0 International (CC BY 4.0)". Below this, it states "This is a human-readable summary of (and not a substitute for) the [license](#). [Disclaimer](#)." The main body is divided into two sections: "You are free to:" and "Under the following terms:". The "You are free to:" section lists two freedoms: "Share" (copy and redistribute the material in any medium or format) and "Adapt" (remix, transform, and build upon the material for any purpose, even commercially). A circular seal on the right says "Free Cultural Works APPROVED FOR". The "Under the following terms:" section lists two conditions: "Attribution" (You must give [appropriate credit](#), provide a link to the license, and [indicate if changes were made](#). You may do so in any reasonable manner, but not in any way that suggests the licensor endorses you or your use.) and "No additional restrictions" (You may not apply legal terms or [technological measures](#) that legally restrict others from doing anything the license permits.).

Attribution 4.0 International (CC BY 4.0)

This is a human-readable summary of (and not a substitute for) the [license](#). [Disclaimer](#).

You are free to:

- Share** — copy and redistribute the material in any medium or format
- Adapt** — remix, transform, and build upon the material for any purpose, even commercially.

The licensor cannot revoke these freedoms as long as you follow the license terms.

Under the following terms:

- Attribution** — You must give [appropriate credit](#), provide a link to the license, and [indicate if changes were made](#). You may do so in any reasonable manner, but not in any way that suggests the licensor endorses you or your use.
- No additional restrictions** — You may not apply legal terms or [technological measures](#) that legally restrict others from doing anything the license permits.

19 April 2024

<https://hdl.handle.net/2440/140624>

JULY 13 2023

Steady-state sound propagation through hot exhaust jets in cooler cross-flow: A computational study

O. Leav ; B. Cazzolato ; C. Howard ; B. Mabrouk



J. Acoust. Soc. Am. 154, 217–231 (2023)

<https://doi.org/10.1121/10.0020069>

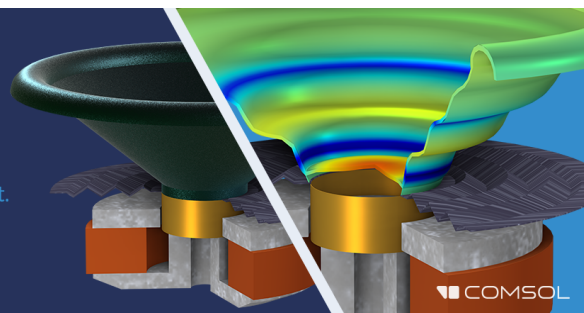


CrossMark

Take the Lead in Acoustics

The ability to account for coupled physics phenomena lets you predict, optimize, and virtually test a design under real-world conditions – even before a first prototype is built.

» Learn more about COMSOL Multiphysics®



COMSOL

Steady-state sound propagation through hot exhaust jets in cooler cross-flow: A computational study

O. Leav,^{1,a)}  B. Cazzolato,¹  C. Howard,¹  and B. Mabrouk²

¹School of Mechanical Engineering, University of Adelaide, Adelaide, Australia

²Laboratoire Roberval, Université de Technologie Compiègne, Compiègne, Cedex, France

ABSTRACT:

An analysis has been carried out to investigate the sound radiation through a heated jet in cooler cross-flow, which is representative of many industrial exhaust systems, using a hybrid steady-state computational fluid dynamics and computational acoustic model. The mean flow and temperature fields are modelled using steady-state computational fluid dynamics, with the turbulence modelled using Reynolds Averaged Navier-Stokes equations. The corresponding mean flow and temperature fields are used in the computational sound propagation model using linearised acoustic wave equation with mean flow based on a scalar flow potential. The results obtained from the computational simulations show that the flow significantly changes the sound propagation path and that the sound levels downstream of the duct outlet are higher than expected from using an acoustic monopole radiation pattern. The dominant mechanism affecting the propagation of sound is the refraction arising from the plume's temperature and velocity gradients. The sound propagation is highly dependent on the proximity from the duct outlet, normalised wavenumber, temperature and the jet to cross-flow mean velocity ratio. This computational study builds upon previous experimental work to analyse the fluid-acoustic interaction for heated jets in cooler cross-flow to understand the complex radiation pattern that leads to higher-than-expected sound levels downstream of the duct outlet.

© 2023 Acoustical Society of America. <https://doi.org/10.1121/10.0020069>

(Received 28 November 2022; revised 17 June 2023; accepted 20 June 2023; published online 13 July 2023)

[Editor: Alan Thomas Wall]

Pages: 217–231

I. INTRODUCTION

Sound propagation from an acoustic source through inhomogeneous media is a complex phenomenon that exists in many systems. An example of this is the radiation of noise from the exit of a duct, which is of particular interest in fields such as aircraft jet exhausts, large heating, ventilation, and air conditioning (HVAC) systems, or large exhaust stacks. An example of radiating duct noise through inhomogeneous media is the noise from an open cycle gas turbine (OCGT) exhaust stack. There is considerable evidence showing that noise levels in the far-field from OCGTs are often higher than predicted.^{1–9} This issue of significant levels of low frequency noise from OCGT has been well-documented,^{1–4,6–10} and can cause annoyance from “throbbing” of high-intensity low frequency noise,² a “beating” sensation in the chest,¹¹ nausea,² and acoustic excitation of structures with low resonance frequencies, such as glass structures and wall panels.²

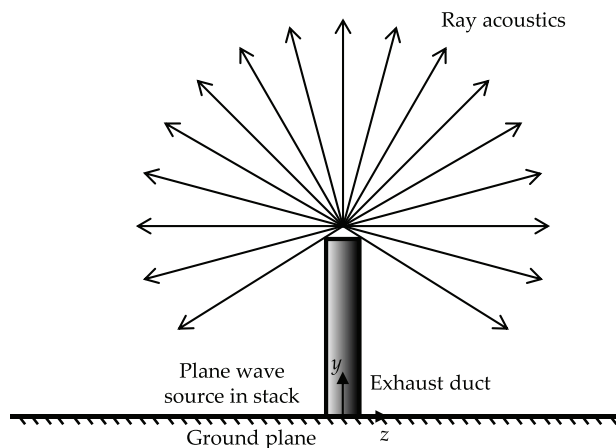
The underprediction of noise levels within communities near OCGT exhaust stacks is hypothesised to be related to the interaction between the sound emitted from the exhaust stack and the fluid dynamics associated with the plume. Earlier work by Björk¹ hypothesises a similar conjecture that a bent-over hot exhaust plume with strong thermal gradients from the plume and changing wind conditions would cause variations in sound levels downstream of up to ± 5 dB in the

neighbourhood. Björk¹ conducted experiments in an attempt to validate his hypothesis by measuring the sound radiation from a full stack with a diameter of 2900 mm, as well as a small scale rig of 145 mm in diameter. Both sets of directivity measurements were in the near-field at $2.9D$, where D is the internal duct diameter, and remained inconclusive.

Research by Leav *et al.*^{12–16} and Cazzolato *et al.*⁵ expanded on the hypothesis by Björk,¹ with numerical and reduced scale experimental studies of OCGT exhaust stack. As a first approximation, an OCGT exhaust stack can be modelled as a jet in cross-flow (JICF), which can be used to investigate the plume's effects on sound propagation. Figure 1 illustrates, through ray acoustics, the expected sound radiation from a low frequency plane wave source within the stack in the presence and absence of the plume. In Fig. 1(a), the sound radiation pattern at low frequencies resembles a monopole source in a homogeneous media, which is a common assumption in predictive models. Further, the presence of a plume in Fig. 1(b) is hypothesised to increase the downstream sound levels as a result of sound refraction. The presence of the atmospheric boundary layer plays a minor role and causes upward refraction of the sound upstream and downward refraction of the sound downstream of the stack. However, this meteorological effect, especially in the presence of temperature inversions is less dramatic and occurs over a much larger domain than refraction through the plume. Leav *et al.*^{12,13} investigated the interaction of sound with the

^{a)}Electronic mail: orddom.leav@adelaide.edu.au

(a)



(b)

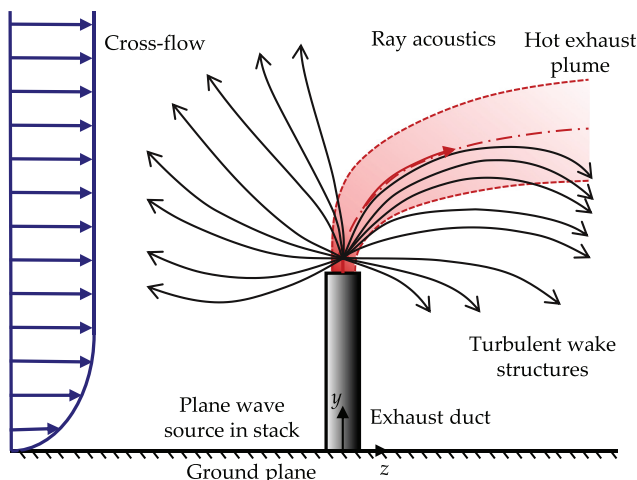


FIG. 1. (Color online) Schematic for the predicted acoustic ray representation of low-frequency sound, where (a) is without the presence of flow and temperature and (b) is with the presence of flow and temperature from an exhaust plume.

thermal gradients associated with a two-dimensional model of a ground-level JICF, and a three-dimensional model of an elevated JICF. Their results showed that whilst radiated sound power is unaffected by the plume, it causes a dramatic redistribution of acoustic energy away from the central axis of the stack, and a significant concentration downwind.

The problem of sound radiation from a hot exhaust jet in a cooler cross-flow has been experimentally investigated by Leav *et al.*^{14–16} and Cazzolato *et al.*⁵ Their experimental study was based on the sound radiation from a reduced-scale model of a 190 MW OCGT exhaust stack undertaken at the Adelaide Wind Tunnel, and found that an acoustic lobe forms downwind of the exhaust stack, and when compared to the scenario with no jet or cross-flow, there is an increase in sound pressure level (SPL) of up to 9 dB downwind. Further work by Leav *et al.*^{15,16} showed that the sound directivity from a hot exhaust jet with cooler cross-flow is strongly dependent on the distance from the duct outlet, acoustic frequency, jet temperature, and cross-flow

momentum flux ratio (cross-flow speed). As the jet temperature increases there is an increase in sound level within the acoustic lobe downwind of the exhaust stack. The cross-flow momentum flux ratio affects the position of the acoustic lobe downwind of the exhaust stack, whereby the highest cross-flow speeds causes the acoustic lobe downwind to refract closer towards ground-level. It should be noted that the results presented by Leav *et al.*^{15,16} are limited to a radius of $28D$ from the duct outlet due to the size of the Adelaide Wind Tunnel, and that refraction was still evident at the measurement ($28D$). The latest work by Cazzolato *et al.*⁵ showed refraction was evident up to $256D$ from the duct outlet of a 250 kW gas turbine. It was found that the geometric spreading was -4.8 dB per doubling in distance downwind, which is less than expected compared with geometric spreading from an acoustic monopole that has -6 dB per doubling in distance. This is significant because it helps to explain why simple propagation models underpredict the sound levels that are measured in practice. Upwind of the stack, it was found that the spreading rate was -6 dB per doubling in distance, and is consistent with models assuming spherical spreading. Outdoor sound predictions commonly use far-field atmospheric sound propagation models, where the meteorological and terrain effects must be considered. There are several review papers on the topic of atmospheric sound propagation models, which use monopole acoustic sources with varying incoming velocity, turbulence, and temperature conditions, that resemble meteorological conditions.^{17–21} While these sound propagation models account for the sound propagation in the far-field, they do not account for a local flow field, such as for the case with an exhaust stack. The exhaust plume will alter the propagation of sound, and the noise source may no longer resemble an elevated monopole, even at very low frequencies.

The effects of local flow and temperature field on sound propagation from exhausts are critical in determining far-field radiation. The gas flow exiting the stack resembles a jet, and there have been various experimental studies into the propagation of sound through jets.^{22,23} It has been shown by Atvars *et al.*²² and Grande²³ that the velocity and temperature of the jet affect the sound directivity, as a result of local sound refraction, resulting in a “cone,” “zone,” or “cusp” of silence being formed along the centreline of the jet. An increase in flow Mach number and temperature of the jet has been shown experimentally to increase the depth of the “cusp.” The subsequent refracted sound leads to the presence of strong lobes to form off-axis, with the angle that the lobe makes with the jet axis increasing with increased temperature and Mach number. These effects are supported numerically by Schubert’s work,^{24,25} who revealed with ray tracing and the wave equation that some of the key features seen in the experimental directivity patterns could be reproduced. These features include the “cusp” of silence and the increase in the SPL of the off-axis acoustic lobe. Mungur *et al.*²⁶ extended this work into a semi-numerical approach with the sound propagation through isothermal jets with varying Mach numbers (0–0.9) and frequencies parameters

($ka = \pi/3 - 8\pi$), where $k = \omega/c$ is the acoustic wavenumber, a is the nozzle radius, and c is the speed of sound. Schubert^{24,25} and Mungur *et al.*²⁶ showed that with an increase in jet Mach number and Helmholtz number (ka), the effects of refraction are more apparent, due to both the increase in velocity gradient and the reduction in the wavelength of sound. The experimental studies by Grande²³ measured the acoustic directivity at a single radius, noting that numerical studies^{24–26} have shown that sound directivity significantly varies with distance from the source.

Further numerical work was undertaken by Astley and Eversman,²⁷ where they used an acoustic finite element (FE) solver to investigate sound radiation from a heated jet, based on the experimental study by Cummings.²⁸ The jet parameters used in the experimental study by Cummings,²⁸ were based on a reduced-scale boiler flue-gas stack and investigated the radiation impedance and transmission loss for an unflanged exhaust duct with a heated exhaust jet ($T_j = 300^\circ\text{C}$). Astley and Eversman²⁷ predicted the refraction of sound from a heated jet at varying directivity radii ($1D < r < 40D$) and a Helmholtz number ($ka = 2$). It is important to note that Astley and Eversman²⁷ neglected the convective flow effects from the jet in their acoustic modelling, and may be justified since, at the jet velocities they examined, the effects of flow on the speed of sound are typically much less than the effects of temperature on the speed of sound.

From the literature reviewed previously, the sound propagating through heated jets is complex. The main focus of these previous studies is to research the sound propagation for jets engines, which have Mach numbers of $M = 0.5$ to 2 ,^{22–26} which are much higher than what is commonly seen in exhaust stacks (where $M = 0.1$). Furthermore, the gas temperatures, in prior research is cooler than what is commonly seen in the exhaust stacks of open cycle gas turbines which can approach 600°C .²⁹

The fluid dynamics of exhaust stack plumes has been researched extensively,^{30–34} and is generally referred to as an elevated jet in cross-flow (JICF). Adaramola *et al.*³⁰ showed that the fluid dynamics associated with an elevated JICF are complicated due to the cross-flow interaction with the stack. The bluff-body flow behind the stack interacts with the plume exiting the duct outlet.^{33,34} A ground-level JICF is a simplification to the elevated JICF,^{33,34} as the stack is removed from this particular case and only the plume is considered.

A typical ground-level JICF schematic is depicted in Fig. 2. The ground-level JICF does not include the interaction of the stack with the cross-flow. Ground-level JICF has been researched extensively both experimentally^{35–41} and numerically.^{42–47} However, research into the resulting acoustic response in the domain has yet to be investigated and is the focus of the work presented here.

Simulations and experiments of jet in cross-flow are affected by the cross-flow momentum ratio, which is the ratio of the momentum of the gas in the jet divided by the momentum of the gas in the cross-flow field. In the geometric near-field, at high cross-flow momentum flux ratios, flow is considered to be jet dominated with the flow exiting the

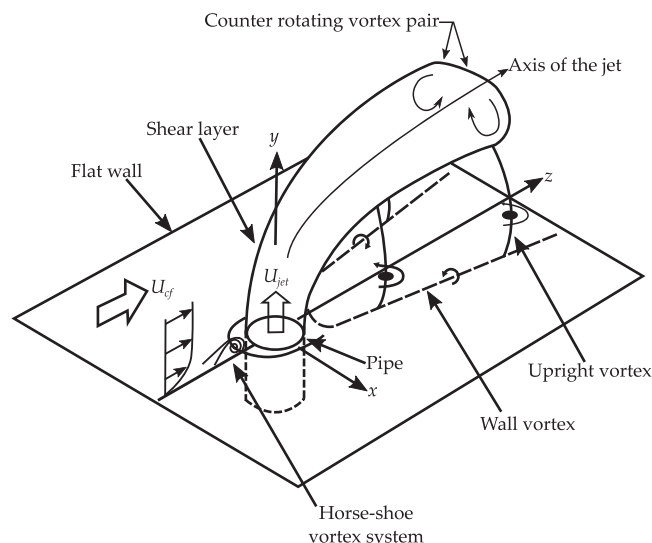


FIG. 2. Schematic of the dominant fluid dynamic structures associated with JICF (Ref. 37).

outlet resembling an axisymmetric jet.³⁶ As the plume develops in the domain, the jet is deflected by the cross-flow momentum. The deflection in the jet then causes the plume to develop into a crescent-like structure.³⁶ In the far-field, the plume then transitions to counter-rotating vortex pairs.³⁶ The counter-rotating vortex pairs become the dominant flow structure in the plume. For high values of jet to cross-flow momentum ratios typically seen in exhaust stacks, the counter-rotating vortex pairs forms earlier in the plume than cases with lower jet to cross-flow momentum ratios.^{36,48}

Steady-state or time-averaged simulations have shown that the plume is symmetrical along a vertical plane along the z -axis (i.e., $x = 0$) in Fig. 2, with the smaller transient features (wake vortices and horseshoe vortices) not being visible in the domain. In the far-field, the dominant steady-state feature of the counter-rotating vortex pairs are plane-symmetric. Rusch *et al.*⁴⁷ showed using computational fluid dynamics (CFD) modelling that for a steady-state ground-level JICF, the smaller transient features, such as the horseshoe vortices and wake vortices are not modelled. By not modelling the smaller transient features, the entrainment of the cross-flow into the plume and enhance mixing in the plume are not adequately modelled leading to higher temperatures in the plume and a higher plume centreline trajectory than transient scale resolving simulations.⁴⁷

In this paper, the effects that a high temperature, exhaust jet, with a cooler cross-flow, has on the propagation of sound are investigated. Steady-state CFD and numerical acoustic simulations, using the finite element method (FEM), are used for the analyses. The layout of the paper is as follows. Section II describes the mathematical models that are utilised for the fluid flow simulations, which involve using CFD and acoustic propagation using the discretised acoustic wave equation with FEM. Section III describes the results from the CFD and acoustic finite element analysis (FEA) simulations. The main conclusions are summarised in Sec. IV.

II. MATHEMATICAL MODELS, DOMAIN, AND BOUNDARY CONDITIONS

The numerical research in this study is conducted with a hybrid computational aeroacoustic scheme that uses both steady-state CFD and the inhomogeneous linearised acoustic wave equation with linear flow potential. Initially, a CFD model of the JICF in FLUENT was generated for the initial mean fluid velocity and temperature. The acoustic FEM was modelled using ANSYS Mechanical for the inhomogeneous linearised acoustic wave equation with linear flow potential.

The simulations conducted in this paper were solved using the University of Adelaide's Phoenix High-Performance Computing cluster. Each simulation used a single node on the cluster, consisting of two Xeon E5-2698v3 central processing units (CPUs), with 2.5 GHz, providing 32 CPUs per node, with each node possessing 128 GB RAM.

A. CFD Modelling with Reynolds Averaged Navier-Stokes (RANS)

Initially, a steady-state CFD analysis in ANSYS FLUENT is conducted to obtain temperature and velocity fields. Modelling the steady-state fluid dynamics related to non-isothermal ground-level JICF, otherwise known as JICF for the rest of the paper. The CFD simulation utilised the RANS model Shear Stress Transport (SST) $\kappa - \omega$ and was chosen on the recommendation of various researchers,^{42–44,47} as it is the most appropriate RANS model for simulating the mixing characteristics in the plume downstream. Rusch⁴⁷ has also shown that accurate predictions of the temperatures downstream of a JICF can be made when using RANS SST $\kappa - \omega$ formulation. To model the temperatures in the plume adequately, the ideal gas law for density and Sutherland's law for dynamic viscosity were implemented to account for the temperature variations. Furthermore, to capture the dynamics of the plume accurately the buoyancy of the gas was modelled. The CFD model uses a second-order upwind spatial discretisation scheme for all its variables and the "Coupled" scheme for the pressure-velocity coupling.

B. Acoustic modelling with FEM

The flow velocity and temperatures modelled by CFD are then mapped onto the FEM for modelling the sound propagation. The numerical acoustic simulations were conducted using a three-dimensional (3-D) linearised acoustic wave equation method that is discretised and solved with FEM. The model was implemented and solved using ANSYS Mechanical.^{49,50} A detailed formulation of the governing equations presented in the following may be found in Leav.¹⁵

It should be noted that there are different acoustic FEMs that could be used for the numerical study. These include the linearised Euler equations, Galbrun's equations, linearised Navier-Stokes, Helmholtz equation and the linearised acoustic wave equation with mean flow using a scalar flow potential. Each FEM listed has its benefits for simulation and careful consideration needs to be taken based on

the assumptions for each acoustic model and the computational requirements to solve higher fidelity models with multiple degrees of freedom (DOF). A benefit of the Helmholtz equation and the linearised acoustic wave equation with mean flow using a scalar flow potential is that these methods are scalar formulation that solves for a single DOF (pressure or scalar velocity potential). In contrast, for a 3-D simulation using the linearised Euler equations, linear Navier-Stokes or Galbrun's equation where there are four or five DOF. It is important to note that the dimensions of the matrices increase in size based on using the square of the number of DOF, and a single DOF for an acoustic FE model significantly reduces the computational resources and computational runtime needed to solve a system, when compared to a higher fidelity model with multiple DOF. Hence, 3-D models with a large number of nodes can be computed with scalar formulations for the acoustic FE method, with limited computational resources and computational runtime, a conclusion supported by Astley and Eversman.²⁷ However, there are limitations with a scalar pressure and scalar flow potential formulation, that needs to be considered when modelling aeroacoustic problems.

The specific implementation of the Helmholtz equation^{27,51,52} and the linearised acoustic wave equation with mean flow using a scalar flow potential⁵³ within ANSYS Mechanical, has been verified, validated and documented by the software vendor ANSYS for numerous acoustic case studies in the literature.^{54–56} Furthermore, Howard and Cazzolato,⁵⁷ and Leav¹⁵ present a number of canonical cases from the literature that have been validated against the commercial package. In particular, Leav¹⁵ has investigated the linearised acoustic wave equation with mean flow using a scalar flow potential for different flow and temperature conditions, which reflects the conditions in this paper. The highest Mach number used in this paper is $M = 0.1$, where Leav¹⁵ validated the linearised acoustic wave equation with mean flow using a scalar flow potential against numerical cases in the literature in the subsonic regime, $M < 0.5$. There is strong evidence in Leav¹⁵ to suggest that the acoustic FE method in this paper using scalar pressure and potential flow is adequate in quantitatively capturing the acoustic pressures when compared to a higher fidelity acoustic FE method, such as the linearised Euler equations, linearised Navier-Stokes, or Galbrun's equation. Hence, at the cost of minor differences in numerical accuracy (noting that with the logarithmic compression associated with calculating dB this is reduced further), a significantly less computationally demanding and time-efficient acoustic FE model can be utilised as a tool to investigate and understand the acoustic interaction with hot-exhaust jets with cooler cross-flow in the far-field ($r = 32D$).

The formulation of the inhomogeneous acoustic wave equation is based on a number of assumptions. The fluid is compressible with relatively no large changes in the bulk pressure. The propagating medium is "frozen" in time with small perturbations in acoustic pressure (the second order and higher order terms are neglected). It is also assumed

that the mean flow and the acoustic perturbations are irrotational. Additionally, it is assumed that the gas is ideal, adiabatic and reversible.

In the analysis to follow, two different acoustic wave equations have been used to accommodate different propagation conditions: a stationary field with only temperature variations permitted, and a formulation which accounts for local temperature and local mean fluid velocity. The following derivation of the acoustic model uses a 3-D formulation in Cartesian coordinates, with four governing equations, namely, the continuity equation, Euler momentum equation, conservation of entropy, and equation of state.

When solving the linearised acoustic wave equation with no mean flow in a stationary field, the Helmholtz equation^{15,49,57} may be used, and is given by

$$\omega^2 \underbrace{\frac{p_a(\vec{x})}{\rho_0(\vec{x})c_0^2(\vec{x})}}_{M_p} + \nabla \cdot \underbrace{\left(\frac{1}{\rho_0(\vec{x})} \nabla p_a(\vec{x}) \right)}_{K_p} = -j\omega \underbrace{Q(\vec{x})}_{f_p}, \quad (1)$$

where $\rho_0(\vec{x})$ is the mean fluid density in kg/m³, $c_0(\vec{x})$ is the speed of sound in m/s, $p_a(\vec{x})$ is the acoustic pressure in Pa, and $Q(\vec{x})$ is the mass source in kg/m³, M_p is the term for the “acoustic fluid mass” for acoustic pressure, K_p is the term for the “acoustic stiffness” for acoustic pressure, and f_p is the “acoustic fluid load” for the acoustic pressure.

The following equations can be used to calculate the local $c_0(\vec{x})$ and $\rho_0(\vec{x})$ as a function of local temperature for an ideal gas medium, respectively,

$$c_0(\vec{x}) = \sqrt{\gamma R_{\text{gas}} T(\vec{x})}, \quad (2a)$$

$$\rho_0(\vec{x}) = \frac{P_{\text{state}}(\vec{x})}{R_{\text{gas}} T(\vec{x})}, \quad (2b)$$

where γ is the ratio for specific heats, R_{gas} is the specific gas constant in J/kgK, T is the absolute temperature in K at position \vec{x} , and P_{state} is the absolute pressure of the gas at a location \vec{x} . Therefore, the governing equation for numerical acoustic simulations with temperature variations in the domain with no flow are given by Eq. (1), using Eqs. (2a) and (2b) in lieu of $\rho_0(\vec{x})$ and $c_0(\vec{x})$, respectively.

The non-stationary formulation for the acoustic wave equation used by ANSYS Mechanical^{49,50} is almost identical to the formulation by Pierce,⁵³ with a slight difference in the final time variant equation that will be discussed later. Pierce⁵³ presents two different formulations for the linearised acoustic wave equation with mean flow using a scalar potential formulation, and the acoustic particle velocity, $\vec{v}_a(\vec{x})$, and acoustic pressure, $p_a(\vec{x})$, are dependent on this definition as shown:

$$\vec{v}_a(\vec{x}) = -\frac{A}{\rho_0(\vec{x})} \nabla \phi(\vec{x}, t), \quad (3)$$

$$p_a(\vec{x}, t) = AD_t \phi(\vec{x}, t), \quad (4)$$

where A is a constant that is related to $\rho_0(\vec{x})$ and $c_0(\vec{x})$. In the derivation by Pierce,⁵³ the author proposes two values of A ; $A = -1$ or $A = -\rho_0(\vec{x})$, which leads to two different formulations of the linearised acoustic wave equation with mean flow using a scalar potential formulation. For the derivation used by ANSYS Mechanical, $A = -1$, and the acoustic velocity, $\vec{v}_a(\vec{x})$, and acoustic pressure, $p_a(\vec{x})$, are given by

$$\vec{v}_a(\vec{x}) = \frac{1}{\rho_0(\vec{x})} \nabla \phi(\vec{x}, t), \quad (5)$$

$$p_a(\vec{x}, t) = -D_t \phi(\vec{x}, t), \quad (6)$$

where $\phi(\vec{x}, t)$ is the velocity potential, and

$$D_t = \frac{\partial}{\partial t} + \vec{v}_0(\vec{x}) \cdot \nabla \quad (7)$$

is the material derivative (or the time derivative following the ambient flow⁵³) and \vec{v}_0 is the mean flow velocity. Further manipulation of the previous terms leads to the derivation for the time dependent non-stationary acoustic wave equation with mean flow, and is given by

$$\nabla \cdot \left(\frac{1}{\rho_0(\vec{x})} \nabla \phi(\vec{x}, t) \right) - D_t \left(\frac{1}{\rho_0(\vec{x})c_0^2(\vec{x})} D_t \phi(\vec{x}, t) \right) = \frac{q(\vec{x})}{\rho_0(\vec{x})}, \quad (8)$$

where $q(\vec{x})$ is

$$q(\vec{x}) = Q(\vec{x}) - \frac{1}{c_0^2(\vec{x})} D_t(\rho_0(\vec{x}) \phi(\vec{x}, t)). \quad (9)$$

ANSYS Mechanical employs Eq. (8) for the time dependent acoustic wave equation taking into consideration the non-stationary mean fluid flow. An important consideration and limitation for the acoustic wave equation given in Eqs. (1) and (8) is that it is assumed that there is no vorticity in the pressure perturbation.

For a harmonic solution of Eq. (8) the velocity potential is introduced:

$$\phi(\vec{x}, t) = \phi(\vec{x}) e^{j\omega t}, \quad (10)$$

whereby substituting Eq. (10) into Eq. (8) and further rearrangement gives the harmonically formulated acoustic wave equation with mean flow

$$\underbrace{\omega^2 \frac{\phi(\vec{x})}{\rho_0(\vec{x})c_0^2(\vec{x})}}_{M_\phi} - j\omega \underbrace{\left(\nabla \cdot \frac{\vec{v}_0(\vec{x})}{\rho_0(\vec{x})c_0^2(\vec{x})} \phi(\vec{x}) + \frac{\vec{v}_0(\vec{x})}{\rho_0(\vec{x})c_0^2(\vec{x})} \cdot \nabla \phi(\vec{x}) \right)}_{C_\phi} - \underbrace{\frac{\vec{v}_0(\vec{x})}{\rho_0(\vec{x})c_0^2(\vec{x})} \vec{v}_0(\vec{x}) \nabla \phi(\vec{x}) + \nabla \cdot \frac{1}{\rho_0(\vec{x})} \nabla \phi(\vec{x})}_{K_\phi} = \underbrace{\frac{q(\vec{x})}{\rho_0(\vec{x})}}_{f_\phi}, \quad (11)$$

TABLE I. Physical parameters for the experimental tests, where parameters with the subscript j corresponding to the jet and subscript cf corresponding to the cross-flow and for a 190 MW OCGT.

Description	Parameter	OCGT Value	Simulation Value	Units
Duct diameter	D	6	0.0476	m
Temperature in duct	T_j	809	300–773	K
Exhaust velocity	u_j	45.2	54.9	ms^{-1}
Mach number	M_j	0.08	0.1	—
Reynolds number	Re_j	3.17×10^6	3.50×10^4	—
Temperature in cross-flow	T_{cf}	300	300	K
Duct height	H_{duct}	60	0.476	m
Acoustic frequency range of interest	f	16–100	1101–2936	Hz
Helmholtz number	ka	0.53–3.19	0.3–0.8	—
Jet to cross-flow momentum flux ratio	R	3–20	5–7.5	—

where M_ϕ is the term for the “acoustic fluid mass” for the acoustic velocity potential, C_ϕ is the term for the “acoustic fluid damping” for the acoustic velocity potential, K_ϕ is the term for the “acoustic fluid stiffness” for the acoustic velocity potential, and f_ϕ is the term for the “acoustic fluid load” for the acoustic velocity potential.

Equations (1) and (11) can be discretised using the Galerkin method for representation using FEM.⁵⁸ Detailed formulation for the discretisation of Eqs. (1) and (11) are provided in the ANSYS Mechanical Manual.⁵⁴ In modelling the sound, the following formulation is used for both the Helmholtz equation without and with mean fluid flow, respectively:

$$(-\omega^2[M_p] + [K_p])\{p\} = f_p, \quad (12a)$$

$$(-\omega^2[M_\phi] + j\omega[C_\phi] + [K_\phi])\{\phi\} = f_\phi, \quad (12b)$$

where $[M]$ is the acoustic fluid mass matrix, $[C]$ is the acoustic damping matrix, $[K]$ is the acoustic stiffness matrix, and f is the acoustic fluid load vector, where subscript p represents

the pressure formulation and subscript ϕ represents the velocity potential formulation. It should be noted that for the case of inviscid flow, the $[C_p]$ is non-existent for the formulation that uses Helmholtz equation without mean fluid flow. Equation (12a) is formulated using pressure p and Eq. (12b) is formulated using the single DOF for the velocity potential ϕ . The acoustic pressure data from Eq. (11) are derived using Eq. (6). The matrix Eq. (12a), is solved directly with the symmetric “Sparse” matrix solver in ANSYS as the matrices have poor numerical conditioning. Similarly, Eq. (12b) is solved directly with the unsymmetric “Sparse” matrix solver in ANSYS, as Eq. (12b) is no longer symmetric with the inclusion of the $[C_\phi]$ term. The matrix formulation for the solver treats the full domain as a matrix which is solved using the “Shared Memory Parallel” mode, which requires less RAM to solve for Eqs. (12a) and (12b) compared with a model with the domain partitioned. Hence, using FEM with ANSYS Mechanical and the “Shared Memory Parallel” mode provides the ability to solve models that have a large number of nodes, a requirement for the accurate propagation of sound through non-isotropic media.

C. Domain and boundary conditions

For the work conducted in the case study, the dimensions for the domain, parameters used for the fluid dynamics and acoustic simulations are based on a reduced scale (1:125) model of a 190 MW OCGT,²⁹ and the experimental work presented in Cazzolato *et al.*,⁵ Leav,¹⁵ and Leav *et al.*^{14,16} These values are presented in Table I.

The geometry of the domain used in the case studies presented in this paper is shown in Fig. 3 and was consistent between the CFD and FEA acoustic simulations. The domain had dimensions $48D \times 48D \times 80D$ ($L_x \times L_y \times L_z$), where $D = 0.0476\text{m}$ is the exhaust duct diameter. This domain is plane-symmetric about the centreline of the duct, with the domain extending $40D$ upstream and downstream of the duct centre, in the direction of the cross-flow free stream. The length of the duct in these simulations is $10D$,

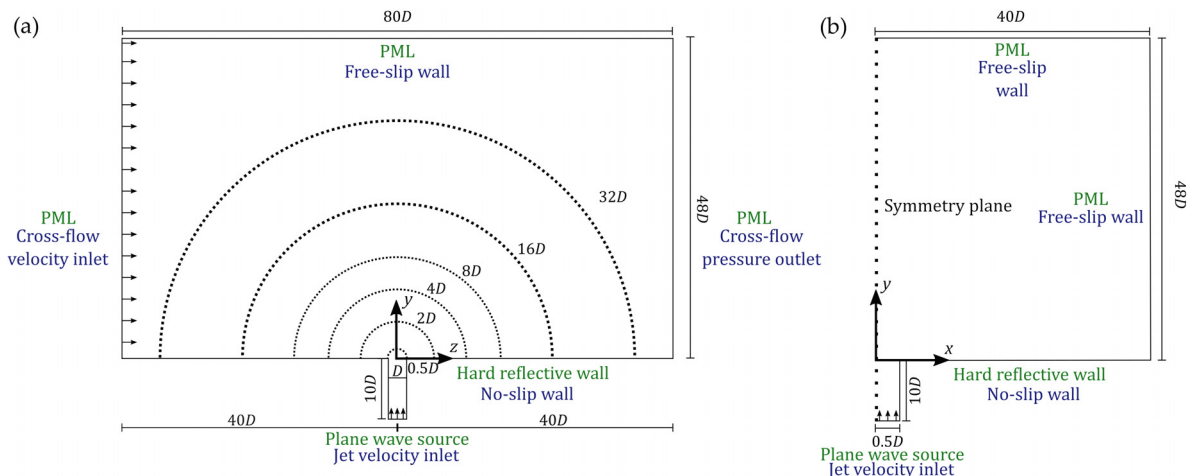


FIG. 3. (Color online) Schematic and dimensions for the simulations, where (a) shows the schematic along the Y - Z plane and (b) shows the schematic along the X - Y plane. The blue text represents the fluid dynamics boundary conditions and green text shows the acoustic boundary conditions.

and was chosen to allow the flow in the duct to develop and to account for the cross-flow effects on the duct outlet, as was shown to occur by Muppidi and Mahesh.⁴⁵ Furthermore, by including the duct itself in the computational acoustic simulations, the effects of diffraction at the edge of the duct outlet and the impedance change at the duct outlet are included.

The CFD mesh was generated using ANSYS and consisted of a fully structured mesh. The elements used are hexahedra “brick” (first order, linear) elements with nodes residing on the vertices. The mesh comprises approximately 9.1×10^6 elements. A mesh independence study was conducted in order to investigate solution convergence, with the results showing that the current domain with 9.1×10^6 elements is sufficient for solution convergence. The results of the mesh independence study are presented in Leav.¹⁵

For the CFD simulations, the jet velocity at the duct inlet, u_j , was Mach $M = 0.1$, and had a fully developed pipe flow velocity profile. The temperature at the duct inlet, T_j , was evaluated at three values: 27 °C (ambient), 250 °C, or 500 °C. The cross-flow velocity, u_{cf} , and the quantitative value at the boundary were chosen to have varying cross-flow free-stream velocity. The velocities for u_{cf} were dependent on the effective velocity ratio, R , equal to the square root of the jet to cross-flow momentum flux ratio, defined as

$$R = \sqrt{\frac{\rho_j u_j^2}{\rho_{cf} u_{cf}^2}}, \quad (13)$$

where ρ_j is the jet density, and ρ_{cf} is the free stream cross-flow density.⁵⁹ In this particular study, two values of R , 5 and 7.5, were chosen as they closely resemble the conditions in real OCGT exhaust stacks. The cross-flow temperature was set 27 °C (ambient). A “non-slip” wall boundary condition was used along the internal duct wall and the “ground” (wall adjacent to the duct outlet). The outlet of the domain was a pressure outlet boundary condition. A “free-slip” boundary condition was used along the centreline symmetry-plane and the remaining walls in the CFD simulations.

The elements used in the acoustic simulation comprised a hybrid mesh with both structured hexahedra “FLUID220” and unstructured tetrahedra “FLUID221.” Both element types have mid-side nodes and are second-order (quadratic) elements. The nodal density of the acoustic simulation was derived using a rule of thumb of 11 nodes per wavelength, λ , at the highest frequency of interest,⁵⁷ which resulted in a node count of approximately 6×10^6 nodes. A mesh independence study has been conducted and showed the solution converged for the sound pressure in an isothermal field, which is presented in detail in Leav.¹⁵

The acoustic simulations used a harmonic velocity source at the base of the duct, with magnitude $u_a = 0.01 \text{ ms}^{-1}$. The frequency for the acoustic source was defined as $ka = \pi f D / c_j$, where f is the acoustic frequency of interest, and c_j is the cross-sectional average speed of sound in the jet. The value of ka for these simulations ranges from 0.3 to 0.8, which typically causes a hemispherical sound

radiation pattern in the absence of the jet or cross-flow. A hard reflective wall boundary condition was used along the internal duct wall, the “ground” wall (the surface adjacent to the duct outlet) and the symmetry-plane. The remaining exterior of the domain contained perfectly matched layer (PML) elements for simulating an infinite acoustic free-field. The PML was at least four elements thick and was larger than one-quarter of the acoustic wavelength (λ) of interest for the simulation, which in this case is a layer that is $4D$ thick.⁵⁷

The results in the acoustic FEM are calculated using acoustic pressure and can be represented using the directivity index (DI), given by⁶⁰

$$\text{DI}(\theta) = 10 \log_{10} \left(\frac{I(\theta)}{I_{av}} \right), \quad (14)$$

where θ is the angular position relative to the vertical, I is the acoustic intensity at θ , and I_{av} is the average acoustic intensity over a hemispherical surface in the acoustic domain. The acoustic intensity for a plane wave, I , can be calculated using the following formulation from Bies *et al.*:⁶⁰

$$I(\vec{x}) = \frac{p_{\text{rms}}^2(\vec{x})}{\rho_0(\vec{x})c_0(\vec{x})}. \quad (15)$$

Bies *et al.*⁶⁰ discuss that Eq. (15) can be used to calculate the intensity in the far-field from a source, where the radius of curvature is ten times the acoustic wavelength. It should be noted that Eq. (15) may not be appropriate in the near-field. A more detailed representation of the coordinate system for DI is shown in Fig. 4. It should be noted that this definition for DI in Eq. (15) is slightly different to the DI presented in Sec. III B 1, and will be discussed later.

In Eq. (14) the average acoustic intensity, I_{av} , can be calculated using Eq. (15) to form the spatial average

$$I_{av} = \frac{1}{N} \sum_{i=1}^N \frac{p_{\text{rms},i}^2(\vec{x})}{\rho_{0,i}(\vec{x})c_{0,i}(\vec{x})}, \quad (16)$$

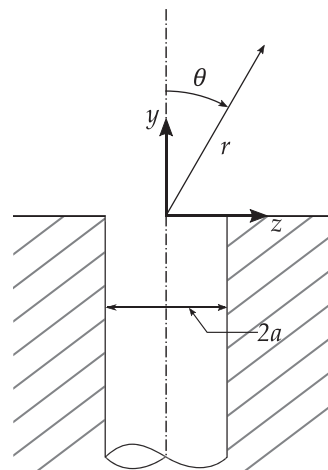


FIG. 4. Schematic for the ground level JICF and the directivity definition from the duct outlet. The quantity a is the duct radius, θ is the directivity angle from the duct centreline, and r is the radius for the directivity arc from the centre of the duct outlet.

where N is the total number of nodes on a spherical surface, and i is the nodal number on the spherical surface. When calculating I_{av} at each radius from the duct outlet a , the spatial average is taken with the expression in Eq. (16), over a quarter-sphere. It should also be noted that for each surface over the quarter-sphere, the nodes are spaced evenly apart and the acoustic intensity at each node has equal weighting in calculating I_{av} .

III. RESULTS AND DISCUSSION

This section discusses the results and key findings from the numerical study. Initially, the steady-state RANS CFD simulation results are presented, which is followed by a discussion on the results from the acoustic FE model simulations with the different propagation conditions: no flow with ambient temperature (or otherwise known as isothermal field), and with temperatures and mean bulk fluid velocities from a CFD simulation of a non-isothermal (heated) JICF. For these cases, three jet temperatures ($T_j = 27^\circ\text{C}$, 250°C , and 500°C), two cross-flow ratios ($R = 5$ and 7.5), and six Helmholtz numbers ($0.2 \leq ka \leq 0.8$) were considered.

A. Non-isothermal jets in cross-flow fluid dynamics

The results presented in this study are from steady-state simulations, and it will be shown that many of the important flow features seen in the literature are successfully reproduced. Figure 5(a) shows a contour plot of the velocity magnitude along the Y - Z plane, and that the jet structure is dominant in the near-field close to the jet outlet adjacent to the ground wall. As the plume develops downwind, the cross-flow causes the jet to deflect, and the plume is bent over. Figure 5(a) also shows that with the development of

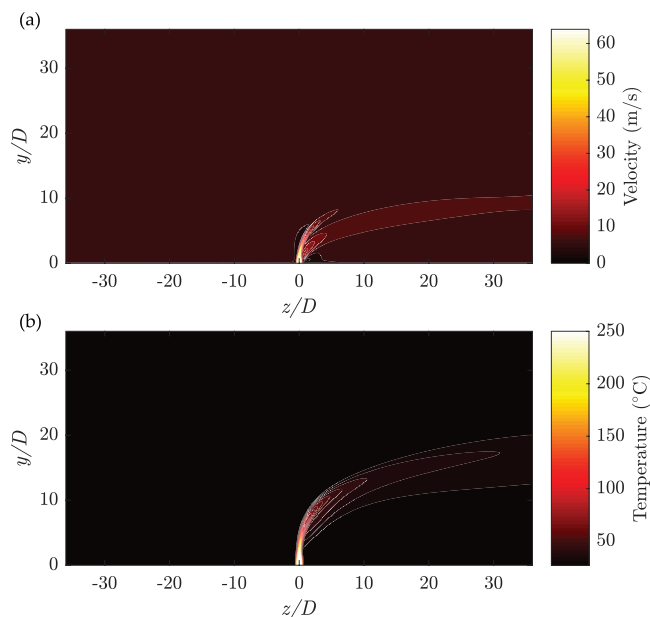


FIG. 5. (Color online) The CFD generated contour plots of (a) flow velocity and (b) temperature along the Y - Z plane (of symmetry), where $T_j = 500^\circ\text{C}$ and $R = 5$. The cross-flow is from left to right.

the plume, a velocity gradient formed by the shear layer develops downwind. Similarly, Fig. 5(b) shows a contour plot of the temperature along the Y - Z plane. There are similar features between the temperature distribution and the velocity magnitude contour plot in Fig. 5(b). Figure 5(b), shows that the elevated temperature follows the deflected plume itself. The highest temperature is observed near the duct outlet, with the temperature of the plume reducing downwind. The decrease in plume temperature is a result of the spatial growth of the plume and the entrainment of the cooler cross-flow.³⁶

Figures 6(a) and 6(b) present the fluid velocity at two locations—in the near-field of the jet and further downstream—and show the span-wise development of the plume. Figure 6(a) indicates that the deflected jet initiates downstream as a “crescent” structure, which is the critical feature of the plume in the near-field. The plume’s “crescent” structure then transitions further to a counter-rotating vortex, which is shown in Fig. 6(b). For the cases studied in this research, it can be seen that the counter-rotating vortex structure is the dominant flow feature downstream, as seen in previous studies.^{35–40,45–47} From the results of numerical simulations conducted here, it can be observed that the increase in cross-flow ratio, R , also causes the formation of the counter-rotating vortex to occur earlier in the plume as it propagates downstream, with the lowest R in the study leading to the “crescent” plume pertaining furthest downstream in all the cases studied. This observation in the spatial formation of the counter-rotating vortex in the plume is consistent with the observations made by Kamotani and Greber.³⁶

Figures 6(c) and 6(d) show the contour plots of the nodal temperature along the X - Y planes at two distances downstream from the jet centreline. As previously observed by Kamotani and Greber,³⁶ the centre of the “crescent” and the counter-rotating vortex contains the hottest region in the plume. This observation of the plume’s temperature was consistent with all the simulations presented in this study.

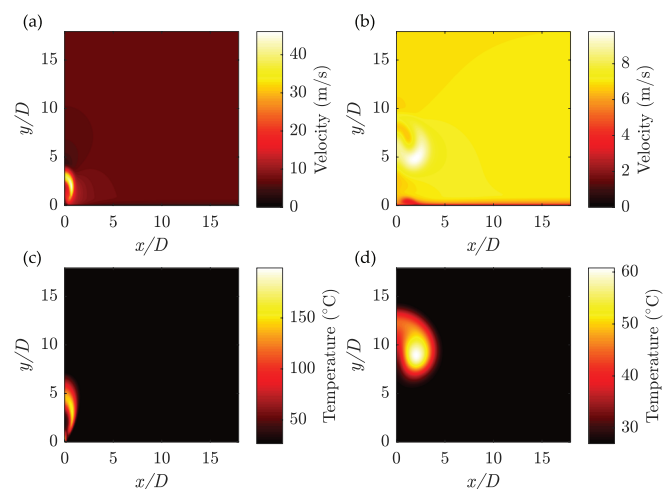


FIG. 6. (Color online) The velocity contour plot along the X - Y plane at (a) $z = 0.5D$ and (b) $z = 8D$, and the temperature contour plots along the X - Y plane at (c) $z = 0.5D$ and (d) $z = 8D$, where $T_j = 500^\circ\text{C}$ and $R = 5$.

Also, observed in the results is a slight increase in the centre temperature of the plume, with an increase in R . This occurs as a result of the reduction in cross-flow momentum, which leads to a lack of cross-flow mixing downstream. The reduction in both the cross-flow momentum and ambient air entrainment downstream also changes the jet trajectory downstream, which is consistent with the observations seen in the previous literature.^{36,41} The change in jet trajectory will also change the position of the thermal and velocity gradient shear layer.

The fluid dynamic structures generated using CFD simulations are very similar in all cases investigated; however, the plume's centreline trajectory changes with varying R . Figure 7 shows the centreline trajectory of the plume with R . The centreline trajectory for the plume was calculated using ANSYS Fluent by tracking a particle that originates from the centre of the duct inlet. For a converged solution, the tracked particle travelled along the plane of symmetry in the domain, which implies the plume is plane-symmetric, which is to be expected for a steady-state simulation for a JICF. An increase in R causes an increase in the height of the plume above the ground-level. The change in plume trajectory is also due to the reduction in cross-flow momentum with the rise in R . Also, shown in Fig. 7 are centreline trajectories for the same R , but with varying jet temperatures, and these show the centreline trajectories are effectively independent of jet temperature.

Since the fluid dynamic results were computed using steady-state simulations and the turbulence was modelled using RANS, the transient turbulent scales were not modelled, as indicated in Sec. II A.

B. Sound propagation

This section presents results from acoustic simulations for two significantly different conditions; the first is for a homogeneous field with no jet, the other is for the heated jet in cross-flow. The results from the CFD simulations are then applied to the nodes in the acoustic FE model. The conditions in the acoustic FE model that were simulated three temperatures, $T_j = 27^\circ\text{C}$, 250°C , and 500°C , two cross-flow ratios, $R = 5$ and 7.5 , and six Helmholtz numbers ($0.3 \leq ka \leq 0.8$) were considered.

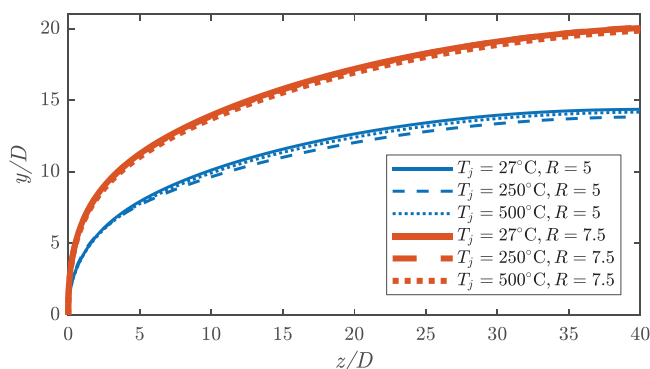


FIG. 7. (Color online) The plume's centreline trajectory for JICF where $R = 5$ and 7.5 , and $T_j = 27^\circ\text{C}$, 250°C , and 500°C .

1. Sound propagation through an isothermal field

Initially, the sound propagation through an isothermal field with constant ambient temperature and in the absence of fluid flow was solved. Two acoustic sources were used: (i) a harmonic velocity source at the outlet which is equivalent to a baffled piston and facilitates comparison against analytical models,⁶⁰ and (ii) a harmonic velocity source at the opposite end of the duct, which is more representative of what happens in practice. The inclusion of the duct with the sound source at the base of the duct changes the acoustic directivity slightly, which will be discussed in this section. The results presented in this section were obtained by solving the acoustic field using Eq. (1), with the acoustic FEM formulation described by Eq. (12a).

Figure 8 presents the sound radiation along the Y - Z plane (of symmetry), at $ka = 0.8$, and is given by Eq. (14). Figure 8 shows the contour plot of the DI along the Y - Z plane of symmetry.

The definition for DI presented in Eq. (14) is used for the results presented in Fig. 8 and is also slightly different compared to the definition of DI for the theoretical baffled piston solution, which is given by

$$DI_{\max}(\vec{\theta}) = 10 \log_{10} \left(\frac{I(\vec{\theta})}{I_{\max}} \right), \quad (17)$$

where I_{\max} is the maximum acoustic intensity in the plot.⁶⁰ In Fig. 9, the DI are plotted as polar line graphs and compared with the theoretical solution for the DI of a baffled piston in an infinite plane at two different Helmholtz numbers ($ka = 0.7$ and 0.8). At these low values of ka , both polar plots in Fig. 9 show similar features where sound is radiated somewhat hemispherically and is axisymmetric, which is expected at low frequencies. At higher frequencies, it would be expected that "lobes" in the directivity pattern would appear, based on the published directivity of a circular piston. Figure 9 shows a good agreement with the DI polar plot results for the theoretical and numerical sound radiation from a baffled piston. The inclusion of the duct produces DI polar results that closely resemble the DI of a baffled piston but with a more concentrated lobe on-axis, along the duct centreline. Additionally, the increase in Helmholtz number,

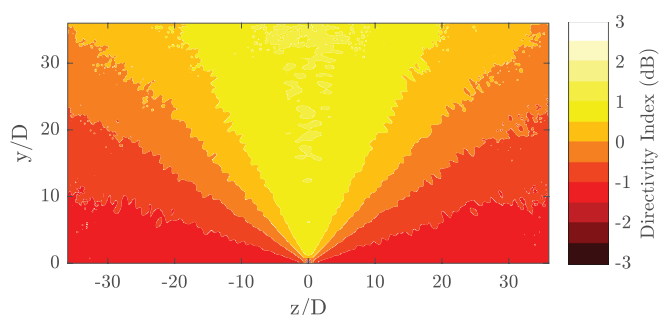


FIG. 8. (Color online) Contour plot of the DI along the Y - Z plane (of symmetry) for sound propagation through the domain in the absence of flow at $ka = 0.8$.

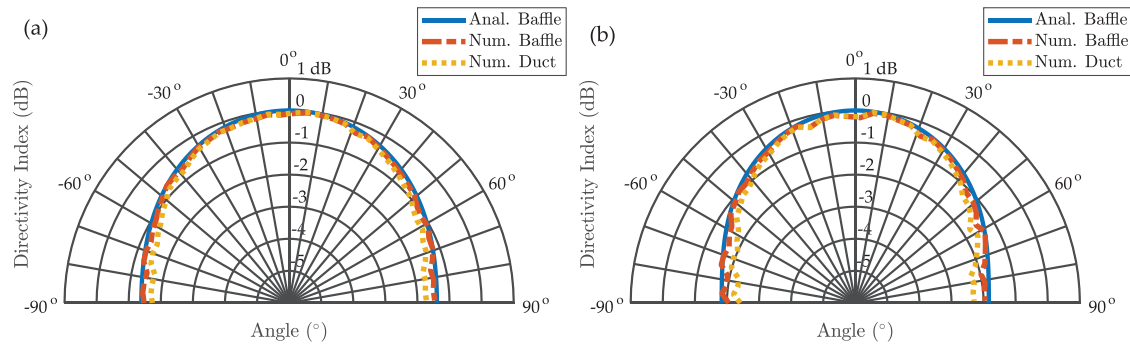


FIG. 9. (Color online) The DI along the Y - Z plane (of symmetry) for sound propagation through the domain in the absence of flow at $r = 32D$, where the results are for (a) $ka = 0.7$ and (b) 0.8 . The results presented are for an analytical expression for a baffled piston, numerical results for a baffled piston, and numerical results for a baffled duct.

ka , from Fig. 9(a) to 9(b) shows the accuracy in the solution reducing slightly as the number of elements per wavelength reduces with increased frequency.

Convergence testing was undertaken, where ultimately the mesh density was limited by the computational hardware. From the acoustic simulations with a pressure formulation [Eq. (12a)] the upper limit for the maximum number of nodes was 12×10^6 . For the velocity potential formulation, the node limit was approximately 6×10^6 . The reason for the difference is due to the solver employed, with the pressure solution using a symmetric solver, and the linear potential solution using an unsymmetric solver. The acoustic results presented in the remainder of this study used a model with a node count of 6×10^6 nodes for consistency.

2. Combining mean convective and thermal effects on sound propagation

Section III B 1 presented benchmark results that do not account for the refraction of sound local to the duct outlet and reflect current models and standards. When accounting for sound refraction in the hot jet, the resulting sound field is very different. The acoustic results in this section will focus on the cases with $R = 5$ – 7.5 , $T_j = 27^\circ\text{C}$ – 500°C , for various ka , and were obtained by solving Eq. (11) and the acoustic FEM formulation described with Eq. (12b).

The superposition of the convective and thermal effects on the sound propagation leads to a distinctive sound

radiation pattern along the Y - Z plane (of symmetry). Figure 10 shows the contour plot of the DI along the Y - Z plane (of symmetry), and shows that in the near-field surrounding the duct outlet, the sound spreads spherically with a constant DI. As the sound propagates and the plume develops, a lobe in the sound field forms downwind of the exhaust, with a DI approximately from 9 to 12 dB. Near the duct centreline axis, a “cusp” forms as a result of the shear layer of the deflected plume, with a drastic reduction in DI and is consistent with previously published works without cross-flow.^{22,23}

Figure 11 shows the DI results as a polar plot along the Y - Z plane (of symmetry) at five different radial distances from the duct outlet ($r = [2D, 4D, 8D, 16D, 32D]$) and $ka = 0.8$. As discussed previously, at a radial distance of $r = 2D$ from the duct outlet, the sound has travelled an insufficient distance for fluid-acoustic interaction to refract and a jet dominated plume leads to an approximately axisymmetric sound directivity pattern, which is approximately hemispherical, with the exception of a slight “cusp” developing. At $r = 4D$, the sound has propagated a sufficient distance to interact with the plume and shows that the acoustic directivity has become asymmetric, with a more pronounced “cusp” at approximately 10° . As the radial distance from the duct outlet increases, the depth of the cusp grows and this

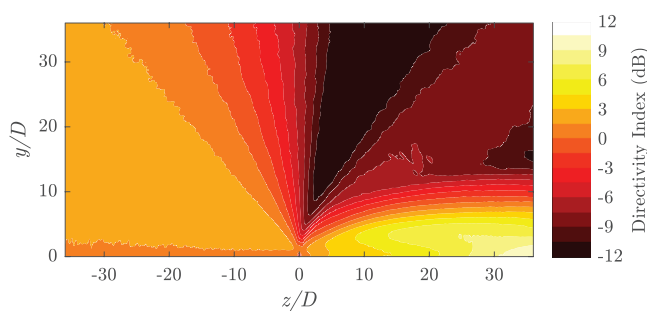


FIG. 10. (Color online) Contour plot of the DI along the Y - Z plane (of symmetry) for sound propagation through the convective and thermal gradients from a JICF with $R = 5$, $T_j = 500^\circ\text{C}$, and $ka = 0.8$. The cross-flow is from left to right. Values less than -12dB are saturated black.

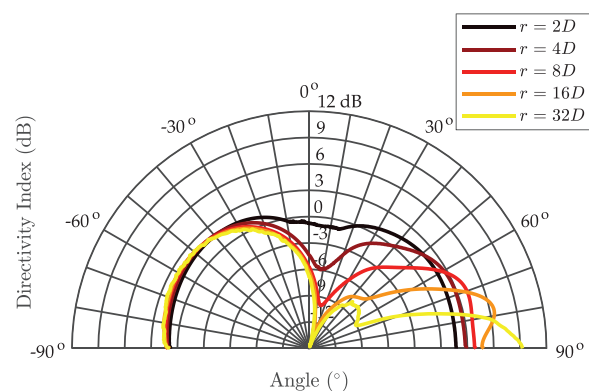


FIG. 11. (Color online) The DI at various distance from the duct outlet ($r = 2D, 4D, 8D, 16D$, and $32D$) along the Y - Z plane for sound propagation through the velocity and thermal gradients from a JICF with $R = 5$, $T_j = 500^\circ\text{C}$, and $ka = 0.8$.

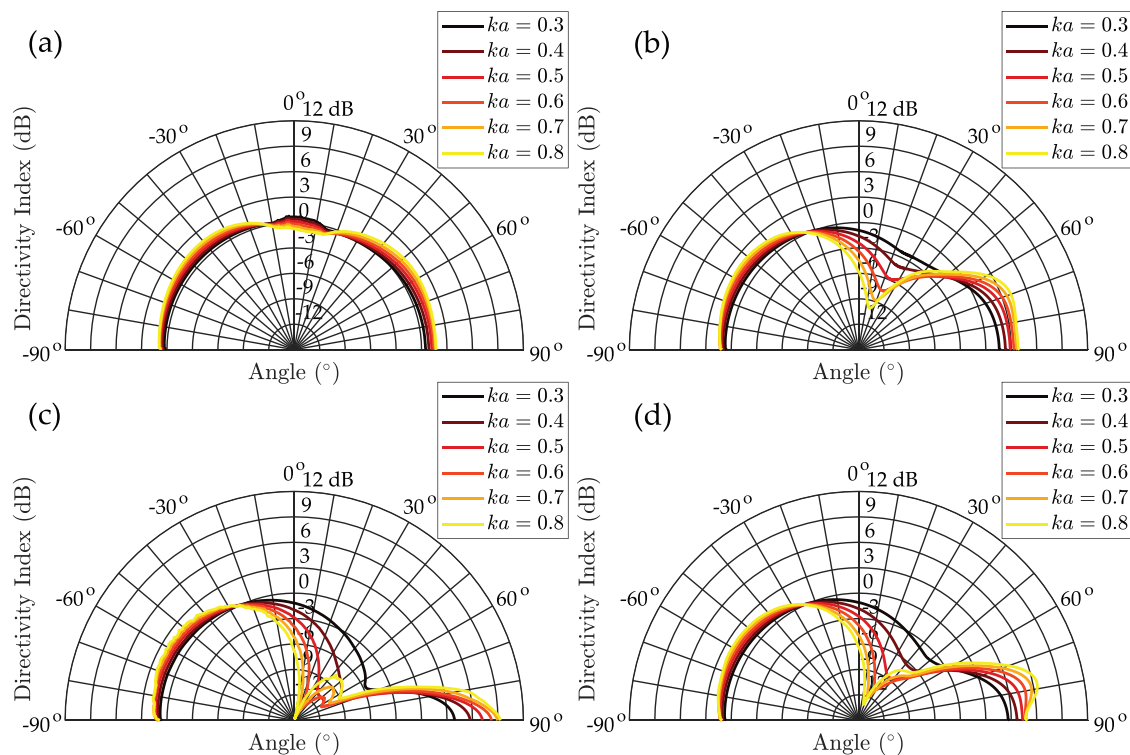


FIG. 12. (Color online) The DI at six different Helmholtz numbers ($ka = 0.3, 0.4, 0.5, 0.6, 0.7$, and 0.8) and at four different radial distances (a) $r = 2D$, (b) $r = 8D$, (c) $r = 16D$, and (d) $r = 32D$. The results are along the Y - Z plane (of symmetry) for sound propagation through the velocity and thermal gradients from a JICF with $R = 5$, and $T_j = 500^\circ\text{C}$. Cross-flow is from left to right.

acoustic energy is redirected towards the horizontal, and predominantly downstream. The directivity at $r = 32D$ shows the largest increase in DI of up to 9 dB.

This observed increase in downwind DI is a result of the plume refracting sound downwards. As previously stated, the effective speed of sound, which governs sound propagation, is mainly influenced by the gas temperature, rather than the steady-state fluid flow; however, the superposition of the two terms has led to a significant increase in downwind DI. Upwind of the duct outlet ($\theta < 0^\circ$) the DI polar plots are approximately elliptical, with the incoming velocity gradient in the boundary layer causing acoustic refraction upwards upwind of the duct outlet, which reduces the DI at ground-level.

The sound propagation is also dependent on wavenumber, ka . Figure 12 shows the DI results as a polar plot at six Helmholtz numbers ($ka = [0.3, 0.4, 0.5, 0.6, 0.7, 0.8]$) and at four different radial distances ($r = [2D, 8D, 16D, 32D]$) along the Y - Z plane (of symmetry). In Fig. 12(a), the radiation pattern is approximately spherical, where the sound has not propagated a sufficient distance to interact with the plume. The directivity plots in Figs. 12(b), 12(c), and 12(d) all exhibit the following similar features that are ka dependent: the increase in downwind DI, a DI “cusp,” and upwind elliptical spreading with upwards acoustic refraction at ground-level. The increase in downwind DI is dependent on the Helmholtz number, where the results for $ka = 0.8$ had greatest increase in DI observed in Figs. 12(b), 12(c), and 12(d). The depth of the cusp in the directivity plots at

$8D$, $16D$, and $32D$ is influenced by ka , with a $ka = 0.8$ producing the deepest cusp.

Figure 13 contains contour plots of the DI along the ground-level (X - Z plane). Figure 13 shows an increase in the downwind DI, and is clearly dominated by the refraction, where the greatest increase in sound level is observed downwind of the exhaust stack at the bottom left corner, with the maximum of 11 dB observed at the boundary of the simulation domain. This is a significant finding and means that an observer on the ground, downwind of an exhaust stack, would experience significantly louder sound levels.

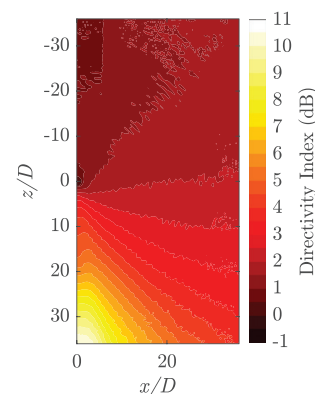


FIG. 13. (Color online) Contour plot of the DI along the X - Z plane (ground-level) for sound propagation through the velocity and thermal gradients from a JICF with $R = 5$, $T_j = 500^\circ\text{C}$, and $ka = 0.8$. The cross-flow is from top to bottom.

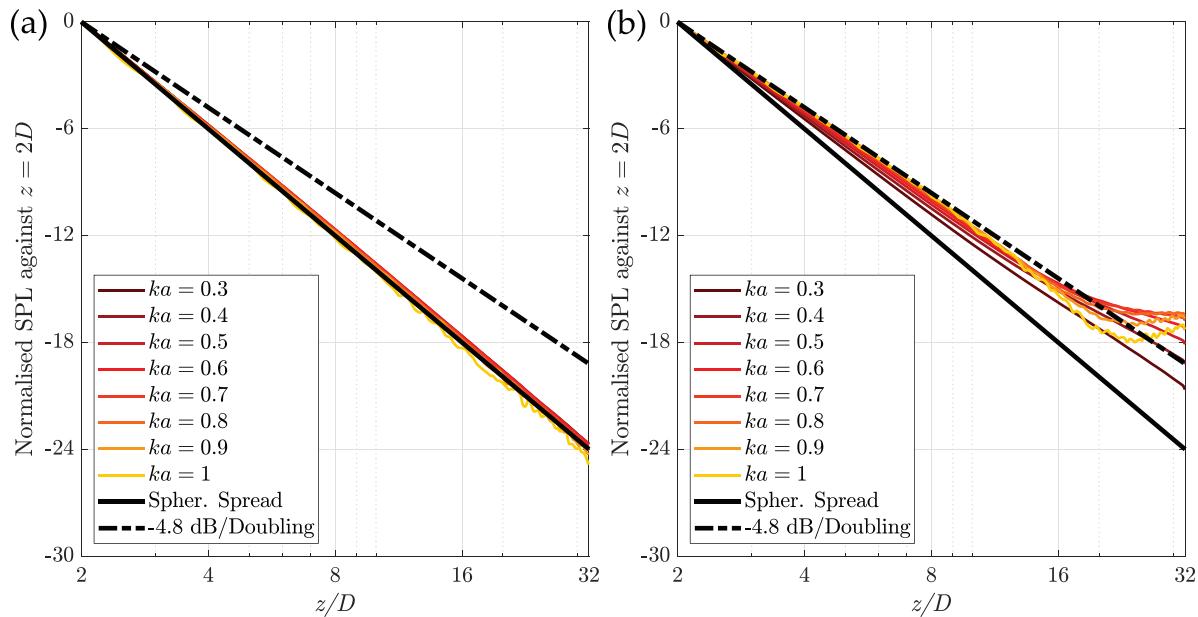


FIG. 14. (Color online) Longitudinal plots of normalised SPL along the Z-axis (line at ground-level and along the plane of symmetry) for (a) upwind of the exhaust, and (b) downwind of the exhaust stack, for sound propagation through the velocity and thermal gradients from a JICF with $R = 5$, $T_j = 500^\circ\text{C}$, and at six different Helmholtz numbers ($ka = 0.3, 0.4, 0.5, 0.6, 0.7$, and 0.8). Geometric spreading rates of -6 dB (spherical) and -4.8 dB (experimentally measured by Cazzolato *et al.* (Ref. 5)) per doubling in distance are plotted for reference.

This phenomenon has been observed in the field by Cazzolato *et al.*⁵

Figure 14 shows the normalised SPL along the Z-axis (line at ground level and along the plane of symmetry) at six different Helmholtz numbers ($ka = 0.3, 0.4, 0.5, 0.6, 0.7$, and 0.8). In Fig. 14(a) the upwind SPLs are normalised against $Z = -2D$, and in Fig. 14(b), the downwind SPL are normalised against $Z = 2D$. These results can be compared against the spherical spreading assumption with 6 dB reduction for every doubling in distance. Observed in Fig. 14(a) are SPLs upwind of the exhaust duct outlet and these results follow closely the spherical spreading assumption. For Fig. 14(b), there is a deviation in the SPLs downwind when compared against the spherical spreading assumption of 6 dB reduction for every doubling in distance. As the frequency increases this deviation in the spherical spreading assumption is more apparent, where at $ka \geq 0.5$ there are non-linear reductions in SPL for distances of $Z \geq 16D$. At $ka \geq 0.7$ there are no reduction in SPL in the far-field ($Z \geq 20D$) with the SPL plateauing for these two frequencies. Moreover, the spreading rate observed from field results presented by Cazzolato *et al.*⁵ of -4.8 dB per doubling in distance coincides with the numerical results, shown in Fig. 14. Therefore, assuming spherical SPL spreading downwind of the exhaust would lead to an underestimation in the predicted SPL downwind of the exhaust stack.

To emphasise the effects of the steady velocity and thermal gradients from non-isothermal ground-level JICF, 3-D directivity radiation plots are compared for four different conditions, which are: an isothermal field with no mean flow, a steady-state temperature field associated with a heated JICF, a steady-state convective flow associated with isothermal JICF, and combined steady-state temperature and

convective fluid flow associated with non-isothermal JICF. The corresponding 3-D directivity radiation patterns are shown in Fig. 15. The acoustic results can be summarised as follows:

- Figure 15(a) shows in the absence of the thermal and velocity gradients imposed from the CFD simulation, the acoustic radiation is axisymmetric, with a slight

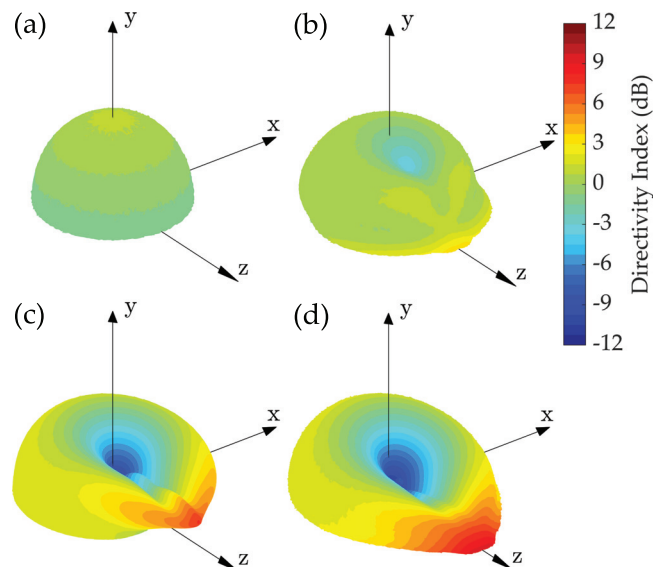


FIG. 15. (Color online) The 3-D directivity radiation pattern for sound propagation through four different cases: (a) homogeneous domain, (b) convective effects, (c) temperature effects, and (d) temperature and convective effects at a radius $r = 32D$ with $R = 5$, $T_j = 500^\circ\text{C}$, $\vec{v}_0 \neq 0$, and $ka = 0.8$. The cross-flow is flowing parallel to the Z-axis, going from left to right. Values of DI less than -12 dB are saturated dark blue.

concentration of acoustic energy along the duct centreline as would be expected from previous published works.

- Figure 15(b) shows the acoustic radiation is no longer axis-symmetric. With the presence of the steady-state velocity from the ground-level JICF, the sound observed downwind of the exhaust stack has been refracted downwards, with an increase in sound observed at ground-level. Upwind of the exhaust stack, the steady-state velocity from the incoming boundary layer shows upwards refraction in Fig. 15(b).
- Figure 15(c) shows the effects of thermal gradients on sound propagation. The sound radiation is now clearly asymmetric. A very distinct lobe has formed just above the horizontal downstream of the duct. The peak in this lobe grows with radial distance and is yet to converge.
- Figure 15(d) shows the combination of both the thermal and convective effects and exhibits the greatest increase in DI downstream of the duct outlet. The convective effect shown in Fig. 15(b) have caused the elevated acoustic lobe in Fig. 15(c) to refract further downwards to be positioned at ground-level, as seen in Fig. 15(d).

The inclusion of both the convective and thermal gradients from non-isothermal ground-level JICF has shown the most dramatic acoustic radiation plot when compared directly in Fig. 15(d), with the “tongue” from the thermal effects observed in Fig. 15(c) pushed onto ground level by the convective effects [Fig. 15(b)].

Figure 16 compares the numerical results for a ground-level JICF at $r = 32D$ against the experimental results for an elevated JICF from Leav.¹⁶ Results are presented for two different directivity radii of $r = 32D$ for the ground-level JICF case and $r = 28D$ for the experimental results. The

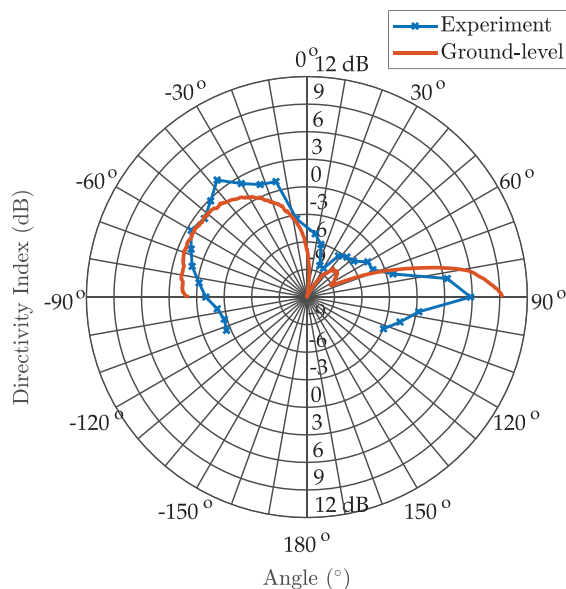


FIG. 16. (Color online) Comparing the DI for the experimental results from Leav (Ref. 16) at $r = 28D$ and one-third octave band with centre frequency of $ka = 0.85$ against the numerical results for a ground-level JICF at $r = 32D$ at $ka = 0.8$. The results are along the Y - Z plane (of symmetry) with $R = 5$, and $T_j = 500^\circ\text{C}$. Cross-flow is from left to right.

results are presented for two slightly different Helmholtz number, a single frequency of $ka = 0.8$ for the numerical results and band-averaged one-third octave band with centre frequency $ka = 0.85$ for the experimental results. Nevertheless, both DI results show qualitative, with broad lobe of approximately 3 dB max DI upwind of the exhaust, a cusp forming near the duct centreline, and an acoustic lobe forming downwind of the exhaust stack. From the experimental results, there is an increase in DI of approximately 6 dB downwind of the exhaust stack, whereas for the numerical results there is an increase in DI of approximately 9 dB. The difference in DI for the acoustic lobe downwind could be related to the difference in geometries, finite number of microphone locations, slightly different temperatures and wave numbers. For the ground level JICF scenario the acoustic lobe downwind would impact the reflected ground plane and increase the DI by up to 3dB, as seen in Fig. 16. Furthermore, the discrepancy in DI could be due to other factors such as: different directivity radii or slightly different Helmholtz number.

The trajectory of the plume is affected by the cross-flow velocity. Figure 17 shows the effects of increasing the plume height by increasing R (i.e., reducing the cross-flow velocity) at a radial distance of $32D$ from the duct outlet. The downstream lobe patterns are clearly visible for $T_j = 250^\circ\text{C}$ and 500°C , and are elevated ($\theta < 90^\circ$) with increasing values of R . For the case of $R = 5$, it can be seen that there is a significant increase in sound level downwind of the duct outlet, along the ground-level, but when R increases to 7.5, the acoustic lobe is elevated above ground-level at approximately 70° . It is clear that R has an impact on the angle of the acoustic lobe downwind. The angle of the “cusp” is around 20° in Fig. 17 and is also dependent on R . For the two values of R investigated in Fig. 17, there is a strong relationship between R and the depth of the “cusp” in the DI polar plot. The increase in jet temperature, T_j , and hence higher thermal gradients leads to an increase in sound refraction and a deepening in the “cusp” in Fig. 17.

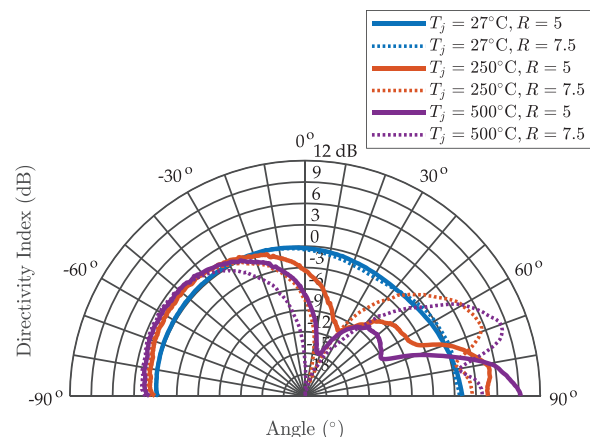


FIG. 17. (Color online) The DI at a radial distance of $32D$ along the Y - Z plane (of symmetry) for sound propagation through a non-isothermal JICF with $R = [5, 7.5]$, $T_j = [27^\circ\text{C}, 250^\circ\text{C}, 500^\circ\text{C}]$, $\vec{v}_0 \neq 0$, and $ka = 0.8$.

From the results in Figs. 15 and 17, it is clear that the jet temperature is a dominant factor in causing the increased downwind DI levels. There is a drastic change in the sound directivity downwind from the refraction of sound from the plume between the homogeneous sound field (which most outdoor noise standards and models use) and the results obtained from these simulations. The change in sound radiation can be explained using the effective speed of sound,

$$c_{\text{eff}} = c + v, \quad (18)$$

where c is the sound speed, and v is the bulk flow speed in the direction of sound propagation.²⁰ The speed of sound, c , can be calculated from the equation

$$c = \sqrt{\gamma_d R_d T (1 + 0.511w)}, \quad (19)$$

where γ_d is the specific heat ratio for dry air, R_d is the gas constant for dry air, T is the absolute temperature, and w is the water vapour mixing ratio.²⁰ Equation (19) shows that the speed of sound is proportional to the square root of absolute temperature. For an exhaust temperature of 500 °C and an ambient temperature of 27 °C, the ratio of the speeds of sound is 1.6. The effects of convective flow on sound propagation is $c_{\text{eff}} = c_0(1 + M)$. Thus, a Mach number of 0.1, the effect of convection is approximately one-sixth of the thermal effect. This is reflected in Figs. 15 and 17, which show an important relationship with the increase in sound observed downwind with the jet temperature, T_j .

IV. CONCLUSION

The results from this study have shown that steady-state convective and thermal gradients found within the plumes of JICF significantly impact the propagation of sound from an exhaust stack. The sound radiation in the absence of steady-state thermal and velocity gradients resembles the directivity pattern for a baffled piston and is spherical at very low frequencies. However, when there is a JICF that has either a steady-state convective flow or is hotter than the ambient gas temperature, or a combination of both, the resulting sound propagation becomes asymmetric, due to the redistribution of acoustical energy, as sound is refracted by the thermal and velocity gradients in the shear layer.

The key results of this study are:

- The directivity of sound is dependent on the distance from the duct outlet, with the directivity near the duct outlet (at $r = 2D$) showing approximately spherical radiation, and at a radial distance of $r = 32D$ the directivity becomes very asymmetric.
- The change in sound propagation path depends significantly on the Helmholtz number, ka , with a higher value of ka more likely to cause the sound to interact with the plume, with an increase in the DI magnitude observed downwind of the stack in the acoustic lobe.

- Upwind of the jet, there is an upward refraction of sound caused by the velocity gradients in the incoming boundary layer.
- The plume causes a strong “cusp” to initially form near the axis of the duct centreline. As the jet is deflected by the cross-flow, the position of the cusp rotates downstream with increasing distance from the stack.
- A dominant factor in sound refraction is the thermal gradient within the plume, which causes a strong “lobe” of sound to form downstream.
- When both the steady-state fluid flow and temperature effects are present, a significant increase in DI of up to 11 dB is observed downwind at ground-level.
- The increase in the downwind DI at ground-level is dependent on the cross-flow ratio, R , where an increase in the cross-flow ratio (decrease in the cross-flow velocity) causes the sound to strike the ground further downwind.

The numerical study has shown that significant sound refraction occurs downwind, as a result of the sound interacting with the hot exhaust plume being deflected by the cooler cross-flow. The refraction of sound downwind leads to the redirection of DI to form an acoustic lobe of increased sound level. Furthermore, the numerical results presented here replicate the salient qualitative and quantitative features observed in the scale experimental tests undertaken on sound radiation from hot exhaust stacks in both a wind tunnel and in the field.^{5,14–16} Hence, practitioners and engineers should account for this when predicting community noise from hot exhaust stacks, such as those found in OCGTs. It is possible that popular models, such as CONCAWE⁶¹ or ISO 9613–2:1996,⁶² will significantly under predict noise level from hot exhaust stacks under certain conditions. For all but directly downwind cases, approximately 3 dB should be added to SPLs compared to monopole sources. However, to account for refraction away from the exhaust centreline for receivers directly downwind up to 12 dB may occur in worst-case conditions.

ACKNOWLEDGMENTS

O.L. was sponsored by an Australian Government Research Training Program Scholarship from 2015 to 2018. This work was supported with supercomputing resources provided by the Phoenix HPC service at the University of Adelaide. This work would not have been possible without the technical expertise from LEAP Australia.

¹E. Björk, “Experimental study of measures to reduce noise radiated from power-station exhaust stacks,” *Noise Control Eng. J.* **42**, 171–178 (1994).

²N. Broner, “A simple criterion for low frequency noise emission assessment,” *J. Low Freq. Noise Vib. Active Control* **29**, 1–13 (2010).

³N. Broner, “A simple outdoor criterion for assessment of low frequency noise emission,” *Acoust. Australia* **39**, 7–14 (2011), available at <https://www.acoustics.org.au/resources/acoustics-australia-journal-archive/>.

⁴N. Broner, “Power to the people,” in *15th International Meeting on Low Frequency Noise and Vibration and Its Control* (Low Frequency Noise, Vibration and Active Control, Stratford upon Avon, UK, 2012), pp. 1–10.

⁵B. Cazzolato, O. Leav, and C. Howard, “Sound directivity from a 250kW gas turbine exhaust system,” in *Acoustics 2021* (Australian Acoustical Society, Wollongong, New South Wales, Australia, 2021), pp. 1–8.

- ⁶G. Hessler, Jr., "Proposed criteria in residential communities for low-frequency noise emissions from industrial sources," *Noise Control Eng. J.* **52**, 179–185 (2004).
- ⁷G. Hessler, Jr., "Proposed criteria for low frequency industrial noise in residential communities," *Low Freq. Noise Vib. Active Control* **24**, 97–106 (2005).
- ⁸R. Hetzel and R. Putnam, "Sources and rating criteria of low frequency gas turbine exhaust noise - via case study," in *Proceedings of INTER-NOISE and NOISE-CON Congress and Conference Proceedings 2009*, Ottawa, Canada (August 23–26, 2009), pp. 1600–1607.
- ⁹G. Kudernatsch, "Combustion turbine exhaust systems-low frequency noise reduction," in *Proceedings of INTER-NOISE 2000, the 29th International Congress and Exhibition on Noise Control Engineering*, Nice, France (August 27–31, 2000), pp. 1–6.
- ¹⁰J. R. Newman and K. I. McEwan, "Low frequency gas turbine noise," *J. Eng. Power* **102**, 476–481 (1980).
- ¹¹N. Broner, "The effects of low frequency noise on people—A review," *J. Sound Vib.* **58**, 483–500 (1978).
- ¹²O. Leav, B. Cazzolato, and C. Howard, "Directivity analysis of sound in turbulent exhaust jets with laminar cross-flow: A numerical study," in *Acoustics 2015* (Australian Acoustical Society, Hunter Valley, New South Wales, Australia, 2015), pp. 1–10.
- ¹³O. Leav, B. Cazzolato, and C. Howard, "A computational analysis of sound directivity from sound propagation through non-isothermal, turbulent exhaust jets in cross-flow," in *Proceedings of the 24th International Congress on Sound and Vibration*, London, UK (July 23–27, 2017), pp. 1–8.
- ¹⁴O. Leav, B. Cazzolato, and C. Howard, "Experimental analysis of sound directivity from sound propagation through non-isothermal, turbulent exhaust jets in cross-flow," in *Acoustics 2018* (Australian Acoustical Society, Adelaide, South Australia, Australia, 2018), pp. 1–10.
- ¹⁵O. Y. Leav, "An investigation into the mechanics of sound propagation through turbulent non-isothermal exhaust jets in cross-flow," Ph.D. thesis, University of Adelaide, Adelaide, Australia (2020).
- ¹⁶O. Leav, B. Cazzolato, and C. Howard, "Sound propagation through elevated, heated jets in cooler cross-flow: An experimental study," *J. Acoust. Soc. Am.* **150**, 82–93 (2021).
- ¹⁷K. Attenborough, S. Taherzadeh, H. Bass, X. Di, R. Raspet, G. Becker, A. Güdesen, A. Chrestman, G. Daigle, and A. L'Espérance, "Benchmark cases for outdoor sound propagation models," *J. Acoust. Soc. Am.* **97**, 173–191 (1995).
- ¹⁸K. Attenborough, "Sound propagation close to the ground," *Ann. Rev. Fluid Mech.* **34**, 51–82 (2002).
- ¹⁹T. Embleton, "Tutorial on sound propagation outdoors," *J. Acoust. Soc. Am.* **100**, 31–48 (1996).
- ²⁰V. Ostashev and D. Wilson, *Acoustics in Moving Inhomogeneous Media* (CRC Press, Boca Raton, FL, 2015).
- ²¹J. Piercy, T. Embleton, and L. Sutherland, "Review of noise propagation in the atmosphere," *J. Acoust. Soc. Am.* **61**, 1403–1418 (1977).
- ²²J. Atvars, L. Schubert, and H. Ribner, "Refraction of sound from a point source placed in an air jet," *J. Acoust. Soc. Am.* **37**, 168–170 (1965).
- ²³E. Grande, "Refraction of injected sound by a very cold nitrogen jet," *J. Acoust. Soc. Am.* **38**, 1063–1064 (1965).
- ²⁴L. Schubert, "Numerical study of sound refraction by a jet flow. I. Ray acoustics," *J. Acoust. Soc. Am.* **51**, 439–446 (1972).
- ²⁵L. Schubert, "Numerical study of sound refraction by a jet flow. II. Wave acoustics," *J. Acoust. Soc. Am.* **51**, 447–463 (1972).
- ²⁶P. Mungur, H. Plumblee, and P. Doak, "Analysis of acoustic radiation in a jet flow environment," *J. Sound Vib.* **36**, 21–52 (1974).
- ²⁷R. J. Astley and W. Eversman, "Wave envelope elements for acoustical radiation in inhomogeneous media," *Comput. Struct.* **30**, 801–810 (1988).
- ²⁸A. Cummings, "High temperature effects on the radiation impedance of an unflanged duct exit," *J. Sound Vib.* **52**, 299–304 (1977).
- ²⁹Siemens, "We power the world with innovative gas turbines—Siemens gas turbine portfolio," Data sheet (2019), <https://assets.new.siemens.com/siemens/assets/api/uuid:ab8578bf-d86f-45d9-a26b-7ac7a274fadd/siemens-gas-turbine-portfolio.pdf> (Last viewed February 7, 2023).
- ³⁰M. Adaramola, D. Sumner, and D. Bergstrom, "Effect of velocity ratio on the streamwise vortex structures in the wake of a stack," *J. Fluids Struct.* **26**, 1–18 (2010).
- ³¹J. Andreopoulos, "Wind tunnel experiments on cooling tower plumes: Part 1—in uniform crossflow," *J. Heat Transfer* **111**, 941–948 (1989).
- ³²J. Andreopoulos, "Wind tunnel experiments on cooling tower plumes: Part 2—In a nonuniform crossflow of boundary layer type," *J. Heat Transfer* **111**, 949–955 (1989).
- ³³O. Eiff, J. Kawall, and J. Keffer, "Lock-in of vortices in the wake of an elevated round turbulent jet in a crossflow," *Exp. Fluids* **19**, 203–213 (1995).
- ³⁴O. Eiff and J. Keffer, "On the structures in the near-wake region of an elevated turbulent jet in a crossflow," *J. Fluid Mech.* **333**, 161–195 (1997).
- ³⁵T. Fric and A. Roshko, "Vortical structure in the wake of a transverse jet," *J. Fluid Mech.* **279**, 1–47 (1994).
- ³⁶Y. Kamotani and I. Greber, "Experiments on a turbulent jet in a cross flow," *Am. Inst. Aeronaut. Astronaut. J.* **10**, 1425–1429 (1972).
- ³⁷R. Kelso, T. Lim, A. Perry, and A. Lim, "An experimental study of round jets in cross-flow," *J. Fluid Mech.* **306**, 111–144 (1996).
- ³⁸R. Kelso, T. Lim, and A. Perry, "New experimental observations of vortical motions in transverse jets," *Phys. Fluids* **10**, 2427–2429 (1998).
- ³⁹S. Sherif and R. Pletcher, "Measurements of the thermal characteristics of heated turbulent jets in crossflow," *J. Heat Transfer* **111**, 897–903 (1989).
- ⁴⁰S. Sherif and R. Pletcher, "Jet-wake thermal characteristics of heated turbulent jets in crossflow," *J. Thermophys. Heat Transfer* **5**, 181–191 (1991).
- ⁴¹L. Su and M. Mungal, "Simultaneous measurements of scalar and velocity field evolution in turbulent crossflowing jets," *J. Fluid Mech.* **513**, 1–45 (2004).
- ⁴²F. Galeazzo, G. Donnert, P. Habisreuther, N. Zarzalis, R. Valdes, and W. Krebs, "Measurement and simulation of turbulent mixing in a jet in cross-flow," *J. Eng. Gas Turbines Power* **133**, 061504 (2011).
- ⁴³F. Galeazzo, G. Donnert, C. Cárdenas, J. Sedlmaier, P. Habisreuther, N. Zarzalis, C. Beck, and W. Krebs, "Computational modeling of turbulent mixing in a jet in crossflow," *Int. J. Heat Fluid Flow* **41**, 55–65 (2013).
- ⁴⁴A. Hoda and S. Acharya, "Predictions of a film coolant jet in crossflow with different turbulence models," *J. Turbomach. Trans. ASME* **122**, 558–569 (2000).
- ⁴⁵S. Muppidi and K. Mahesh, "Study of trajectories of jets in crossflow using direct numerical simulations," *J. Fluid Mech.* **530**, 81–100 (2005).
- ⁴⁶S. Muppidi and K. Mahesh, "Two-dimensional model problem to explain counter-rotating vortex pair formation in a transverse jet," *Phys. Fluids* **18**, 085103 (2006).
- ⁴⁷D. Rusch, L. Blum, A. Moser, and T. Roesgen, "Turbulence model validation for fire simulation by CFD and experimental investigation of a hot jet in crossflow," *Fire Safety J.* **43**, 429–441 (2008).
- ⁴⁸P. Schlatter, S. Bagheri, and D. Henningson, "Self-sustained global oscillations in a jet in crossflow," *Theor. Comput. Fluid Dyn.* **25**, 129–146 (2011).
- ⁴⁹ANSYS, *ANSYS Mechanical APDL Theory Reference*, 18th ed. (ANSYS, Inc., Canonsburg, PA, 2017).
- ⁵⁰ANSYS, *ANSYS Mechanical APDL Acoustic Analysis Guide*, 18th ed. (ANSYS, Inc., Canonsburg, PA, 2017).
- ⁵¹P. Bergmann, "The wave equation in a medium with a variable index of refraction," *J. Acoust. Soc. Am.* **17**, 329–333 (1946).
- ⁵²G. Ross and R. C. Chivers, "A note on the Helmholtz equations for acoustic waves in inhomogeneous media," *J. Acoust. Soc. Am.* **80**, 1536–1539 (1986).
- ⁵³A. Pierce, "Wave equation for sound in fluids with unsteady inhomogeneous flow," *J. Acoust. Soc. Am.* **87**, 2292–2299 (1990).
- ⁵⁴ANSYS, *ANSYS Mechanical APDL Theory Reference* (ANSYS, Inc., Canonsburg, PA, 2023).
- ⁵⁵ANSYS, *Technology Showcase: Example Problems* (ANSYS, Inc., Canonsburg, PA, 2023).
- ⁵⁶ANSYS, *Ansys Mechanical APDL Verification Manual* (ANSYS, Inc., Canonsburg, PA, 2017).
- ⁵⁷C. Howard and B. Cazzolato, *Acoustic Analyses Using MATLAB® and Ansys®* (CRC Press, Boca Raton, FL, 2014).
- ⁵⁸K.-J. Bathe, *Finite Element Procedures* (Klaus-Jürgen Bathe, Englewood Cliffs, NJ, 2006).
- ⁵⁹S. Smith and M. Mungal, "Mixing, structure and scaling of the jet in crossflow," *J. Fluid Mech.* **357**, 83–122 (1998).
- ⁶⁰D. Bies, C. Hansen, and C. Howard, *Engineering Noise Control: Theory and Practice*, 5th ed., edited by C. Press (CRC Press, Boca Raton, FL, 2017).
- ⁶¹K. Marsh, "The CONCAWE model for calculating the propagation of noise from open-air industrial plants," *Appl. Acoust.* **15**, 411–428 (1982).
- ⁶²ISO 9613-2:1996, "Acoustics—Attenuation of sound during propagation outdoors – Part 2: General method of calculation" (International Organization for Standardization, Geneva, Switzerland, 1996).